

# Hydromechanical Rock Mass Fatigue in Deep-Seated Landslides Accompanying Seasonal Variations in Pore Pressures

Giona Preisig<sup>1</sup> · Erik Eberhardt<sup>1</sup> · Megan Smithyman<sup>2</sup> · Alexander Preh<sup>3</sup> · Luca Bonzanigo<sup>4</sup>

Received: 31 October 2014 / Accepted: 2 January 2016 / Published online: 16 January 2016  
© Springer-Verlag Wien 2016

**Abstract** The episodic movement of deep-seated landslides is often governed by the presence of high pore pressures and reduced effective stresses along active shear surfaces. Pore pressures are subject to cyclic fluctuation under seasonal variations of groundwater recharge, resulting in an intermittent movement characterized by acceleration–deceleration phases. However, it is not always clear why certain acceleration phases reach alarming levels without a clear trigger (i.e., in the absence of an exceptional pore pressure event). This paper presents a conceptual framework linking hydromechanical cycling, progressive failure and fatigue to investigate and explain the episodic behavior of deep-seated landslides using the Campo Vallemaggia landslide in Switzerland as a case study. A combination of monitoring data and advanced numerical modeling is used. The principal processes forcing the slope into a critical disequilibrium state are analyzed as a function of rock mass damage and fatigue. Modeling results suggest that during periods of slope acceleration, the rock slope experiences localized fatigue and gradual weakening through slip along pre-existing natural fractures and yield of critically stressed intact rock

bridges. At certain intervals, pockets of critically weakened rock may produce a period of enhanced slope movement in response to a small pore pressure increase similar to those routinely experienced each year. Accordingly, the distribution and connectivity of pre-existing permeable planes of weakness play a central role. These structures are often related to the rock mass's tectonic history or initiate (and dilate) in response to stress changes that disturb the entire slope, such as glacial unloading or seismic loading via large earthquakes. The latter is discussed in detail in a companion paper to this (Gischig et al., *Rock Mech Rock Eng*, 2015). The results and framework presented further demonstrate that episodic movement and progressive failure of deep-seated landslides cannot be analyzed by means of classical limit equilibrium tools but require advanced numerical models. When calibrated against slope monitoring data, the improved understanding of episodic slope movements can lead to more reliable early warning forecasting and improved landslide hazard management.

**Keywords** Deep-seated landslides · Brittle fracture damage · Fatigue · One-way coupled hydromechanical modeling · Campo Vallemaggia

✉ Giona Preisig  
gionapreisig@outlook.com

<sup>1</sup> Geological Engineering, Department of Earth, Ocean and Atmospheric Sciences, The University of British Columbia, 2207 Main Mall, Vancouver, BC V6T 1Z4, Canada

<sup>2</sup> Golder Associates Ltd, 4260 Still Creek Drive, Burnaby, BC V5C 6C6, Canada

<sup>3</sup> Institute of Geotechnics, Vienna University of Technology, Karlsplatz 13/203, 1040 Vienna, Austria

<sup>4</sup> geolog.ch SA, viale Stazione 16A, 6500 Bellinzona, Switzerland

## 1 Introduction

Episodic downhill movement of deep-seated landslides in rock slopes results from the combination of intrinsic material creep, slip along existing fractures, and plastic deformations arising from brittle fracture processes. Intrinsic material creep is governed by gravitational loading and is responsible for viscoplastic rock matrix flow under constant stress but also through microfracturing when the deviatoric stress is high enough to cause failure

(Goodman 1980). Elasto-plastic and brittle deformations within the fracture network govern the macroscopic kinematics and are usually driven by a modification of the stress field (Eberhardt 2008). One major modification is the decrease of effective stresses in fractures due to increasing pore pressures. This reduces their frictional strength and promotes slip, which in turn may cause the slip and dilation of adjacent fractures and/or the rupture of intact rock bridges. Furuya et al. (1999) and Bonzanigo (1999) were able to quantify a critical slip threshold for borehole water levels (i.e., pore pressures) in their respective studies of the Zentoku landslide, Japan, and Campo Vallemaggia landslide, Switzerland. Below the critical water level, only small movements were observed to occur associated with steady-state creep. Above the critical level, pore pressures were seen to trigger a period of accelerating downslope movement (Fig. 1a). In some cases, this accelerating behavior results in a sudden and catastrophic failure event, for example the Vaiont landslide, Italy (Müller 1964, 1987; Selli et al. 1964; Hendron and Patton 1985; Kilburn and Petley 2003); in other cases, periods of accelerating

displacements eventually subside and return to background levels, for example, the Kilchenstock, Switzerland (Heim 1932; Löw 1997). The results are problematic for early warning forecasting where accelerating slope displacements are taken as a sign of imminent failure. The velocities encountered are variable, with base velocities typically ranging between mm/year and cm/year, and peak velocities between cm/year and m/year (Fig. 1).

Leroueil et al. (1996) have proposed the subdivision of the history of an unstable slope into four stages: (1) pre-failure, (2) first-time failure, (3) post-failure, and (4) reactivation. Within the context of rock slopes in Alpine environments, first-time failures are often related to periods of glacial retreat where substantial slope over-steepening, stress unloading, and kinematic de-buttressing occur. Reactivation phases can then be associated with modifications of the stress field, for example, through cyclic variations of pore pressures within the slope or seismic loading through earthquakes.

Such repeated fluctuations of stresses may result in a slow weakening and degradation of the rock mass, i.e., fatigue. This implies the modification of the rock mass

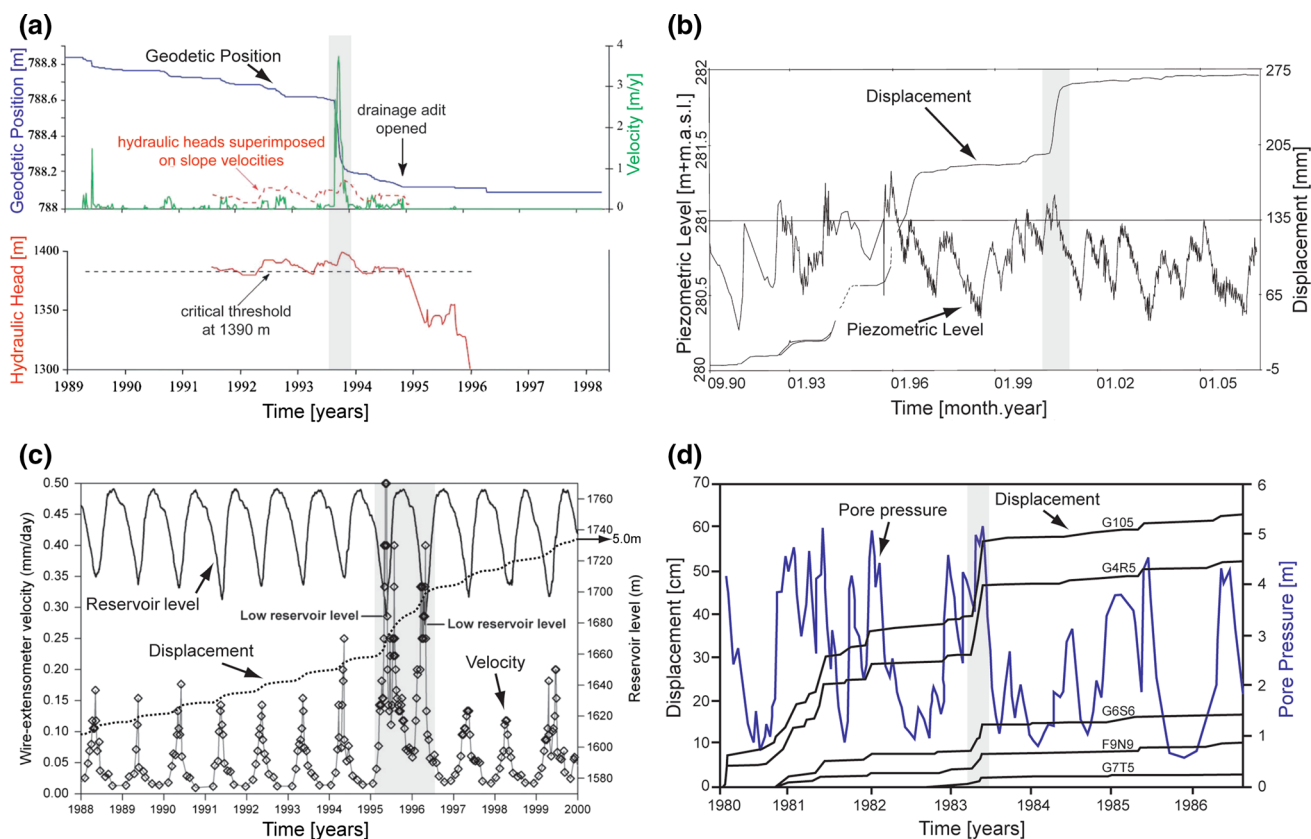


**Fig. 1** Time-dependent movement of four different deep-seated landslides. **a** Campo Vallemaggia landslide, Ticino, Switzerland, involving crystalline rocks (after Bonzanigo et al. 2007; Eberhardt et al. 2007), **b** Brewery Creek landslide, Clyde Dam reservoir, New Zealand, involving schist (after Macfarlane 2009), **c** Hochmais-

Atemkopf landslide, Northern Tyrol, Austria, involving crystalline rocks (after Zangerl et al. 2010), **d** Sallèdes landslide, Auvergne, France, involving marlstone (after Vuillet and Hutter 1988). *Superimposed gray intervals* indicate substantial landslide acceleration events without exceptional triggering events

properties, both, mechanical and hydraulic, with time, forcing a rock slope into a critical disequilibrium condition with periods of enhanced accelerations (Eberhardt 2008). This concept is presented in Figs. 1 and 2. In Fig. 1, the movement histories of four different landslides relative to various measures of groundwater pressures or reservoir levels are plotted as a function of time. Several periods of accelerating behavior are highlighted with gray shading that coincide with periods of increased but not exceptional rises in pore pressure. It is hypothesized here that these events are accompanied by localized rock mass yielding and slip, and that this “damage” accumulates with time and number of load cycles.

Cyclic fluctuations in (effective) stress may arise both naturally and in response to anthropogenic influences; these can vary considerably in terms of recurrence frequency and stress change amplitudes (Table 1; Fig. 2a). For example, seasonal variations in pore pressures associated with changing groundwater levels during snowmelt or intense rainfall periods occur on an annual/bi-annual cycle and represent an intermediate stress-change event. The resulting strength degradation is referred to here as *hydromechanical fatigue*. A similar periodicity and stress change occurs in response to fluctuating water levels in reservoirs for conventional hydroelectric power generation (e.g., Zangerl et al. 2010), although these fluctuations are largely concentrated along the foot of the slope. Seasonal warming and cooling fluctuations also occur on an annual cycle but are localized to the surface and shallow, open tension cracks. It can be noted though, that *thermomechanical fatigue* has been cited as contributing towards

rock slope deformations; e.g., Checkerboard Creek, Canada (Watson et al. 2004), Randa, Switzerland (Gischig et al. 2011). Less frequent but more substantial in terms of damage potential are earthquakes, which generate substantial stress changes that disturb the entire slope. In a companion paper, Gischig et al. (2015) demonstrate how a sequence of earthquakes can bring a strong rock mass to catastrophic failure in an incremental manner by inducing increasing damage and deformation (i.e., *seismic fatigue*) until kinematic conditions change to enable mobilization. These key mechanisms involved in the episodic movement and fatigue of rock slopes are summarized in Fig. 2a, while Fig. 2b presents two conceptual plots illustrating displacement and accumulated damage as a function of time. In Fig. 2b the curve for cumulative damage as a function of time is assumed to be comparable to that of slope displacements. As demonstrated later in this paper, this is exhibited in numerical modeling results (see also Gischig et al. 2015). Initially, substantial rock mass damage may be linked to glacial unloading and kinematic de-buttressing of glacially oversteepened slopes (Eberhardt 2008; Pedrazzini et al. 2013; Leith et al. 2014). Hydromechanical and thermomechanical fatigue are then responsible for episodic movement and progressive weakening of the rock mass (Bonzanigo 1999; Bonzanigo et al. 2006, 2007; Gischig et al. 2011). The monitoring period indicated in Fig. 2b mimics the cases reported in Fig. 1. Finally, a seismic event might occur and generate considerable damage leading to a toe breakout or ultimate slope collapse, as assumed for the Sierre landslide in Switzerland (Pedrazzini et al. 2013).

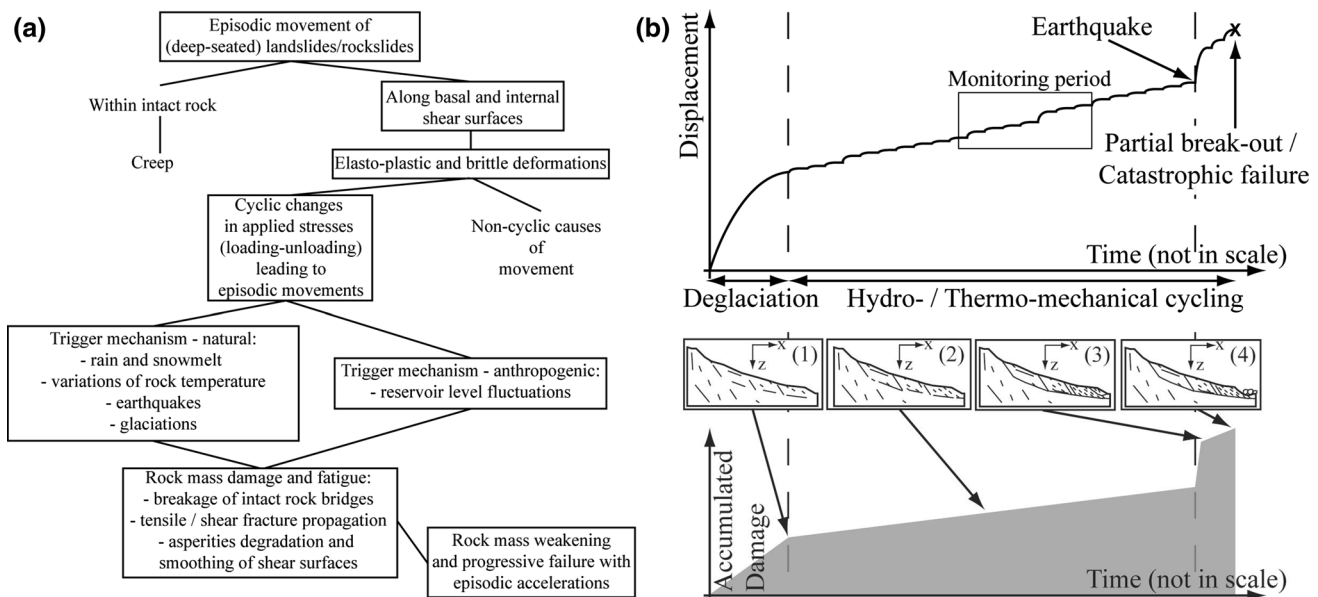


**Fig. 2** a Flowchart illustrating the sources of rock mass fatigue within deep-seated landslides, and b conceptual plots illustrating the displacement and accumulated damage time response resulting from the different types of rock mass fatigue

**Table 1** Examples of different types of fatigue mechanisms potentially affecting deep-seated landslides

Fatigue mechanism	Factor	Trigger mechanism	Frequency	Loading rate	Amplitude of stress change (MPa)	Spatial distribution	Example references
Hydro-mechanical	Groundwater pressure (effective stress) fluctuations	Seasonal precipitation: rainfall and snowmelt	Semi-annual to annual	Seasonal	0.1–0.5	Distributed at depth	Bonzanigo et al. (2007)
	Anthropogenic water pressure fluctuations	Reservoir level fluctuations	Semi-annual to annual	Seasonal	0.1–0.5	Local at foot of slope	Zangerl et al. (2010)
		Pumped-storage hydroelectricity	Daily	Daily	<0.1	Local at foot of slope)	Harby et al. (2013)
Thermo-mechanical	Thermal stress variations	Seasonal variations of rock temperature	Semi-annual to annual	Daily	>1	Distributed across surface	Gischig et al. (2011) and Watson et al. (2004)
Seismic	Stress changes induced by seismic waves	Earthquake	Decades to centuries	Several seconds	0.4–0.5 ( $M \sim 6.0$ at 30 km distance)	Disturbs entire slope	Gischig et al. (2015)
Glacial	Glacial loading and unloading	Glaciation	Tens of thousands of years	Millennial	5–20	Disturbs entire slope	Eberhardt et al. (2004) and Leith et al. (2014)

For hydromechanical fatigue, a groundwater flow causing significant pore pressure variations is required. These conditions may be satisfied in crystalline rock masses by the presence of deep confined aquifers related to fractured and faulted rock (Bonzanigo 1999; Parriaux et al. 2010). Here, hydrodynamic parameters continuously evolve because of the dependency of fracture permeability on effective stress, shear slip, aperture and dilation (Min et al. 2004; Hsiung et al. 2005; Preisig et al. 2012). In alpine valleys, pore pressures in a slope aquifer are usually increased two times per year: (1) in Spring due to snow melt, often accompanied by heavy rainfall; and (2) in Fall because of intense rainfall periods (Parriaux et al. 2010; Hansmann et al. 2012). These pore pressure fluctuations are typically in the range of 0.01–0.05 MPa for soil slopes, and 0.1–0.5 MPa for rock slopes (Bonzanigo 1999; Parriaux et al. 2010).

In this work, we investigate the role played by hydromechanical rock mass fatigue in reactivation stages of the episodic movement and progressive failure of a deep-seated landslide. A key objective is to resolve the dominant processes behind signals of rock slope fatigue (manifested as unexpected acceleration episodes) that occur in the absence of a triggering event of exceptional amplitude. The well-known landslide of Campo Vallemaggia in southern Switzerland is used as an illustrative case study. This deep-seated landslide provides over 100 years of historical slope movement data, together with a decade of more recent pore pressure and displacement

data. Advanced numerical modeling is used together with these data sets to simulate deep-seated fatigue processes and intermittent slope displacements over long time intervals, in order to better understand and interpret early warning monitoring data. The paper is divided into three principal sections. First, the Campo Vallemaggia deep-seated landslide is briefly described. The second section then presents the methodology and the numerical models used to investigate hydromechanical fatigue. Finally, a discussion of the results and conclusions are provided.

## 2 The Campo Vallemaggia Deep-Seated Landslide

Only the principal characteristics of the Campo Vallemaggia landslide are reported here. For a detailed description, the reader is referred to Bonzanigo (1999), Bonzanigo et al. (2006, 2007) and Eberhardt et al. (2007).

### 2.1 Slide Geology

The Campo Vallemaggia deep-seated landslide is located in the Canton Ticino in the southern Swiss Alps, north of the city of Locarno. It involves a moving mass of 800 million m<sup>3</sup> of weathered and fractured crystalline rocks, which prior to stabilization works in 1995, had contributed to a history of: (1) damage to homes and infrastructure in the villages of Campo Vallemaggia and Cimalmotto situated on top of the slow moving slide, and

(2) blocking of the Rovana di Campo river at the toe of the landslide (Fig. 3). The slide mass is composed of a weathered metamorphic series of amphibolites, schists, gneiss, metaperidotites, and metacarbonates, overlain by a thin layer of Quaternary deposits (Bonzanigo et al. 2007). Bonzanigo (1999) identified several major sub-vertical tectonic faults oriented NNW–SSE (red dashed lines in Fig. 3), as well as a series of E–W scarps (orange dashed lines in Fig. 3) and open tension cracks arising from past slope movements. Minor structures include two dominant joint sets. The more frequent and persistent set is parallel to the schistosity with a dip direction of  $145^\circ$  (SE) and a dip angle of  $20^\circ$ – $30^\circ$ . The less frequent set, dips sub-vertically at  $70^\circ$ – $80^\circ$  to the N and E. The geometry of the basal sliding zone is sub-parallel to the first of these, dipping between  $20^\circ$  and  $30^\circ$  and reaching depths of up to 300 m. Internal shear surfaces, together with the tectonic faults, form a complex system of interdependent blocks (Fig. 3), whose boundaries govern the slope kinematics, deformations and displacements. In these regions, the rock mass is highly damaged, weathered and permeable. This might be the result of hundreds if not thousands of years of movement induced by the fluctuation of pore pressures. The most prominent feature is that of a major sub-vertical NNW–SSE fault, labeled “dividing fault” in Fig. 3, which effectively divides the landslide into two separate interacting slide bodies: the Campo Vallemaggia and Cimalmotto bodies (Fig. 4). The movement of the Cimalmotto

body is kinematically constrained by the Campo Vallemaggia body and depends on its movement. Table 2 summarizes the measured and back-calculated rock mass properties assessed during the landslide characterization investigations by Bonzanigo (1999) and Bonzanigo et al. (2007).

## 2.2 Slide Hydrogeology

Within the landslide, deep groundwater flow occurs along confined and artesian intervals of increased fracture permeability below and adjacent to the basal sliding zone (see cross section in Fig. 3). These produce high volumetric flow rates (more than 30 L/s of artesian flow rate was initially measured during the drilling of a deep borehole) and high pore pressures (up to 3 MPa in the deepest interval), and are connected to the surface through the subvertical NNW–SSE striking faults. Multiple artesian springs can be found aligned along such structures (see Bonzanigo et al. 2007). Hydraulic heads in the monitoring boreholes roughly reach their lowest levels in winter, increase in spring due to snow melt, slightly decrease in summer, and increase again in autumn due to rainfall which is particularly intense at that time of year for the Locarno region. This results in observed annual pore pressure fluctuations of up to 0.25 MPa. However, as noted by Bonzanigo (1999) and Bonzanigo et al. (2007), the relationship between precipitation patterns and pore

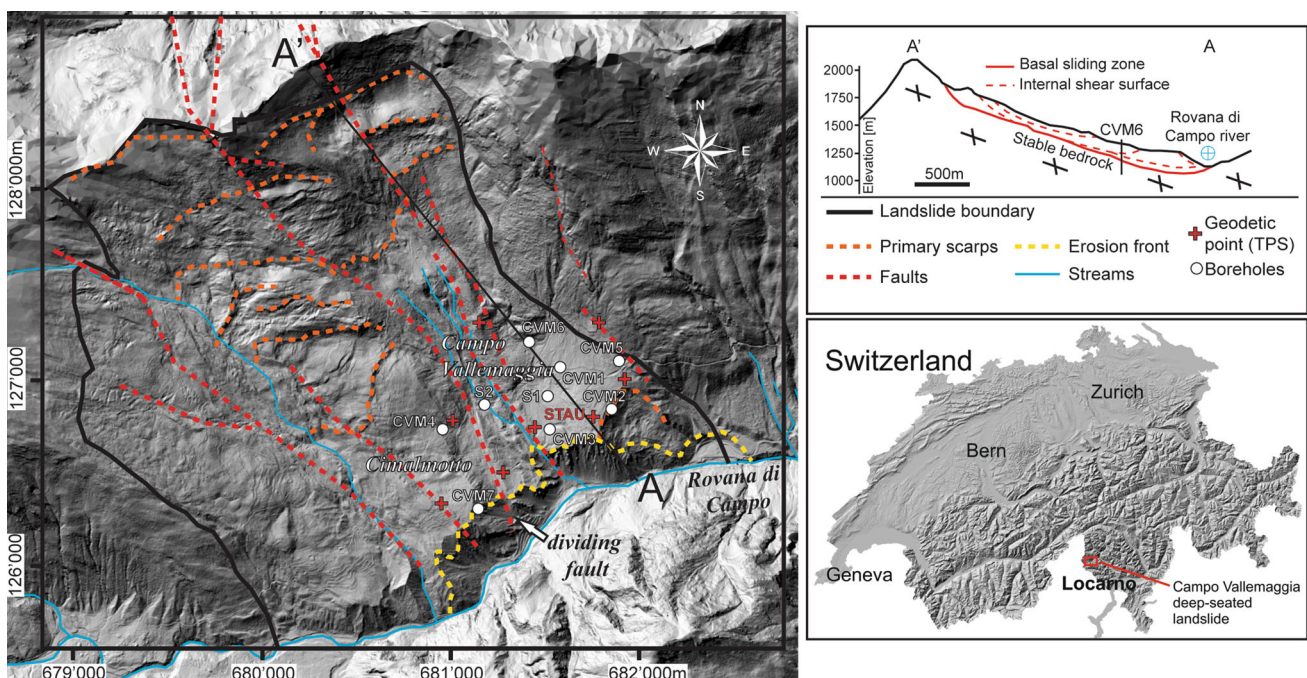


**Fig. 3** Digital elevation model of the Campo Vallemaggia deep-seated landslide with principal geological and geomorphologic features, observation boreholes and geodetic monitoring points.

Insets include a cross section showing the basal and internal shear surfaces (modified from Bonzanigo et al. 2007), and a map of Switzerland locating Campo Vallemaggia

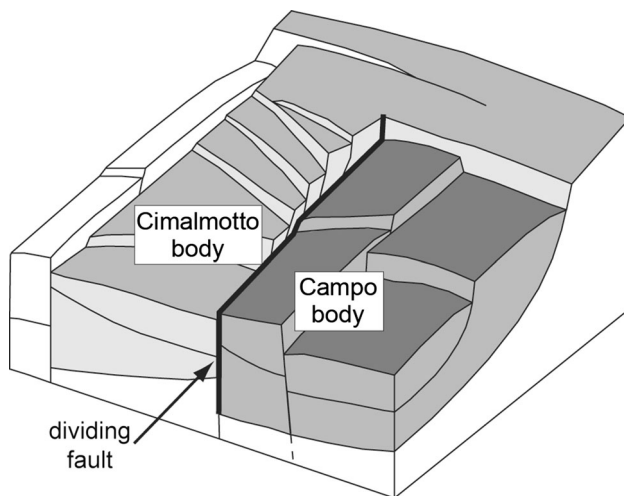


**Fig. 4** Three-dimensional model illustrating the separate but interacting bodies constituting the Campo Vallemaggia deep-seated landslide. The **black bold line** identifies the dividing fault which separates the Campo and Cimalmotto slide bodies (modified from Bonzanigo et al. 2007)

pressure fluctuations is not unique, principally because the catchment area of the Campo Vallemaggia landslide is extensive and incorporates different complex groundwater flow paths. Indeed, the increase of deep pore pressures is characterized by a time lag relative to heavy precipitation events, confirming that the landslide involves a very large catchment area and is recharged by a deep flow system.

### 2.3 Acceleration Events

Seasonal increases in pore pressures were seen to coincide with landslide accelerations from mm-cm/year baseline velocities to peak velocities in the range of 0.1–1 cm/day (Bonzanigo et al. 2006). Bonzanigo et al. (2007) summarize the landslide history between 1780 and 1993 during which several crisis periods were recorded (average interval between crises is about 20–25 years). Many of these acceleration events reached peak velocities in the range of 1–10 cm/day (3.7–37 m/year) and were reported as extraordinary and unexpected; i.e., they did not coincide

**Table 2** Measured and back-calculated geotechnical properties for the principal rock mass units comprising the Campo Vallemaggia deep-seated landslide (after Bonzanigo 1999)

Property (units)	Value	Source
Density, $\rho_r$ (kg/m <sup>3</sup> )	2230–2270	Borehole S1—unstable rock mass
	2160–2570	Borehole S2—unstable rock mass
	1800–2100	Borehole CVM7—unstable rock mass
Hydraulic conductivity, $K$ (m/s)	$2 \times 10^{-7}$	Borehole S1, Lugeon test in the unstable rock mass
	$2 \times 10^{-5}$ – $1 \times 10^{-4}$	Hydraulic tests in borehole CVM4 in areas of artesian inflows (deep confined aquifer)
	$10^{-8}$ – $10^{-6}$	Borehole CVM7
Uniaxial compressive strength, $UCS$ (MPa)	110	Gneiss Occhiadino (CVM4–CVM6)
	90	Schistose Gneiss (CVM4–CVM6)
	100–220	Amphibolitic Gneiss (CVM4–CVM6)
	200–260	Metaperidotite (CVM4–CVM6)
Frictional angle, $\phi$ (°)	32–35	CVM7 (disturbed material)
	25–30	Intact gneiss (along schistosity plane)
	45	Intact gneiss
	20–25	Schist (along schistosity plane)
Cohesion, $c$ (kPa)	30–40	Completely weathered rock
	10–50	CVM7 (disturbed material)
	1000	Intact gneiss
	200	Schist
Elastic modulus, $E$ (GPa)	30	Completely weathered rock
	30	Intact gneiss
	1	Schist
Consolidation modulus, $M$ (GPa)	0.1	Completely weathered rock
	4–8	CVM7 (disturbed material)

with an exceptionally intense precipitation or snow melt period relative to previous years. Moreover, several exceptional precipitation years between 1780 and 1993 did not trigger any remarkable acceleration events. Bonzanigo (1999) and Bonzanigo et al. (2007) invoke a pulsing behaviour related to the effect of the opening of fractures and subsequent quick drainage to explain the intermittent movement of the deep-seated landslide. This observation is compatible with the hypothesis of hydromechanical fatigue as introduced here.

The detailed hydrogeological and geomechanical characterization of the Campo Vallemaggia landslide presented in Bonzanigo (1999) was facilitated by seven deep boreholes providing multipoint pore pressure and inclinometer deformation profiles. This was supplemented by a network of geodetic monitoring points on surface (Fig. 3). Based on these data, mitigation strategies were developed including the excavation of a drainage adit in the stable rock mass below the basal sliding zone (see Eberhardt et al. 2007 for a detailed description). From the adit, a series of multiple radial boreholes were drilled upwards into the confined aquifer sectors coincident with the basal sliding zone. A water level drawdown of up to 200 m (2 MPa) was measured in the observation boreholes before and after drainage. This resulted in the stabilization of the Campo slide body (Figs. 1a, 4), which in turn stabilized the neighboring Cimalmotto slide body. The pressure depletion resulted in a localized ground settlement of 0.5 m above the drainage adit (for more details see Bonzanigo 1999; Bonzanigo et al. 2007; Eberhardt et al. 2007). This is probably one of the world's largest measured ground settlements associated with groundwater depletion in crystalline fractured rocks (Preisig et al. 2014).

### 3 Numerical Analysis of Hydromechanical Fatigue

#### 3.1 Methodology and Workflow

The study of rock mass fatigue and intermittent movements in natural rock slopes require analyses that consider: (1) large spatial scales, (2) long time periods, (3) brittle fracture damage, and (4) fracture flow. Discontinuum-based numerical techniques such as the distinct-element method (Cundall and Hart 1992) are able to explicitly simulate brittle fracture and fracture flow; however, fully-coupled hydromechanical discontinuum models are prohibitively time consuming for the spatial and temporal scales required (Preisig et al. 2012, 2015). As an alternative, their advantages can be utilized if simplifying assumptions are adopted. In the context of deep-seated landslides, one acceptable simplification is to neglect modifications in pore pressure associated with stress changes. Another is to

consider hydrodynamic parameters, such as the hydraulic conductivity, specific storage coefficient and porosity, as constants. These conditions imply that deformations do not modify the hydrodynamic behaviour of the unstable slope except for the opening of new flow paths in response to fracturing of intact rock bridges. This reduces the hydromechanical interactions to a one-way coupling in which changing pore pressures can influence slope deformations through changes in effective stress and stress-induced rock mass damage. This is our starting strategy for simulating the slope movement patterns observed at Campo Vallemaggia. At this point, it is important to reemphasize that the objective of the numerical modeling is not to perform a detailed back-analysis of Campo Vallemaggia (see Eberhardt et al. 2007 for this), but to instead develop a conceptual framework linking hydromechanical cycling, progressive failure, and fatigue to the episodic behavior of deep-seated landslides.

To do so, the fluctuations in pore pressures over time were first modeled using a transient groundwater flow simulator. Modeled pore pressures were then imported into a distinct-element model to simulate the geomechanical response of the deep-seated landslide. The duration of both models is a 50 year time window. Output quantities from the distinct-element model that were analyzed for fatigue effects included: slope displacement/velocity and number of failed rock bridges over time. Details regarding these two independent numerical models are described below.

##### 3.1.1 Finite Element Groundwater Flow Analysis

The 3-D transient groundwater flow simulation was carried out using the finite element software Ground Water (Cornaton 2014). The principal assumption of this model is that the deep-seated landslide is only recharged by water from its surface. This assumption is in part an oversimplification because as previously noted and indicated in Bonzanigo (1999), deep groundwater recharge plays an important role in the occurrence of pore pressures observed at depth. However, lateral and deep flow contributions are difficult to introduce in the model due to the absence of measured data. Moreover, the surface recharge assumption limits the model domain to the landslide area (black line in Fig. 3), and is justified by the fact that the groundwater flow analysis is being used to reproduce the magnitude of pore pressures and their fluctuations over time and not the groundwater flow system in detail.

The model geometry incorporates a thick aquitard representing the sliding rock mass, which confines a thin layer representing the deep fractured aquifer system located beneath the basal sliding zone (Fig. 5a). The geometry of the basal sliding zone was constructed from a kriging map of the landslide thickness developed from seismic

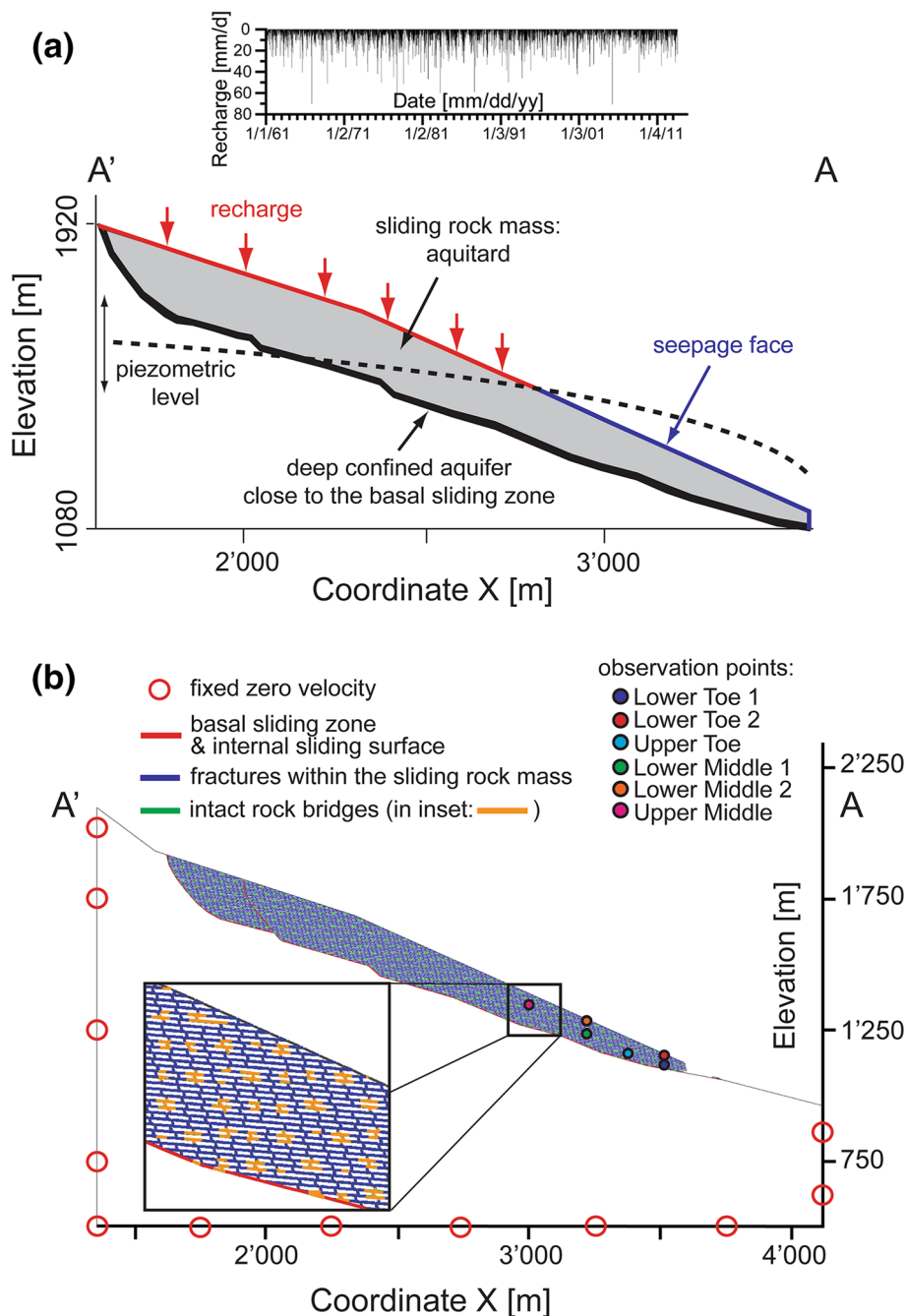
refraction and reflection data, together with borehole data reported in Bonzanigo (1999) and Bonzanigo et al. (2007). Note that for simplification, complex structures such as scarps and sub-vertical faults were not introduced.

Nodes along the modeled slope surface were assigned the following boundary conditions:

(1) A time series of groundwater recharge developed from rain and snow data for the period 1961–2011, illustrated at the top of Fig. 5a. These data were extracted from the database CLIMAP-net of MeteoSwiss for the

meteorological station of Bosco Gurin, located a few km north of Campo Vallemaggia. (2) A seepage face condition. With this boundary condition, groundwater exits the model where the simulated piezometric surface is higher than the topographic (model) surface, as shown by the blue line in Fig. 5a. In comparison, the imposed recharge function (boundary condition 1) is effective at nodes where the piezometric surface is lower than the topographic surface, as indicated by the red line in Fig. 5a. The specified boundary conditions and the imposed recharge time series

**Fig. 5** Modeling of hydromechanical fatigue. **a** Model geometry and boundary conditions used in the groundwater flow model. **b** Model geometry, boundary conditions and location of observation points used in the geomechanical model. The 2-D cross sections coincide with section A–A' in Fig. 3. *Inset in b* shows the rock mass discretization including natural fractures (blue segments), intact rock bridges (orange segments) and the basal sliding zone (red segments)





leads to seasonally fluctuating modeled pore pressures, piezometric levels and infiltration/exfiltration zones (Fig. 5a). Note that processes in the unsaturated zone are neglected and assumed to be insignificant within the scope of this work.

The transient flow model is run for a period of 50 years where pore pressure fields are computed within the unstable slope at a time interval of 14 days. The simulation is calibrated against measured hydraulic heads of Bonzanigo (1999) in the period 1991–1997 by fitting the hydrodynamic parameters. The initial values of hydraulic conductivities and specific storage coefficients are based on the measured and back-calculated values of Bonzanigo (1999) (Table 2). It is important to note that the drainage adit opened in 1995 and its effects on the pore pressure field are not included in the model; i.e., the analysis focuses on the history of instability in the slope. Moreover, deep boreholes have shown that groundwater flow is largely limited to deep confined zones at the base of the Campo Vallemaggia landslide (Bonzanigo 1999; Bonzanigo et al. 2007). Thus, only computed pore pressures close to this deep structure are imported and considered in the geomechanical analysis.

### 3.1.2 Distinct-Element Slope Deformation, Brittle Fracture and Fatigue Analysis

The 2-D commercial distinct-element program UDEC (Itasca 2013) was used to perform the geomechanical fatigue analysis. As previously mentioned, the main assumption regarding the treatment of the hydromechanical interactions is that they can be reduced to a one-way coupling. Under these conditions, each computed pore pressure field can be imported in sequence into the geomechanical model to simulate 50 years of slope response to pore pressure fluctuation and the corresponding development of fatigue and progressive failure.

The model geometry was taken along cross section A–A' in Fig. 3. Based on field observations by Bonzanigo (1999), the model includes: (i) a stable bedrock below the sliding mass; (ii) a basal sliding zone (red line in Fig. 5b); (iii) a major scarp in the upper half of the slide body acting as an internal shear surface; (iv) a pre-existing network of natural fractures (blue segments in insets of Figs. 5b, 6) replicating those observed in the slide body, consisting of a persistent set of sub-horizontal fractures parallel to schistosity with a spacing of 5 m (Set 1 in Fig. 6), and a non-persistent set of cross-cutting sub-vertical fractures with a 15 m spacing (Set 2 in Fig. 6); and lastly (v) a series of intact rock bridges between the natural fractures, which serve as potential fracture pathways if their strengths are exceeded by localized changes in the effective stresses (orange segments in insets of Figs. 5b, 6).

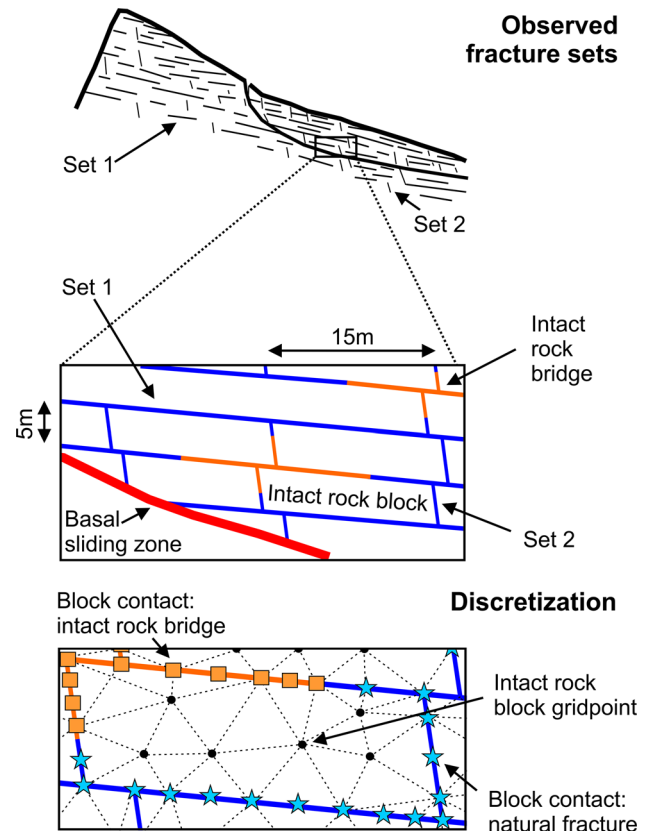


**Fig. 6** Upper part fracture sets observed in the field with a more frequent and persistent set parallel to the schistosity (*Set 1*) and a less frequent and persistent sub-vertical set (*Set 2*) (modified from Bonzanigo 1999). Lower part discretization in the geomechanical model: (i) the middle inset illustrates the implemented fracture geometry with (in blue) persistent sub-horizontal natural fractures (*Set 1*), non-persistent sub-vertical natural fractures (*Set 2*) and (in orange) segments mimicking intact rock bridges. (ii) The lower inset details how a non-divisible intact rock block is treated in the distinct-element model with gridpoints capturing the linear-elastic behaviour and contacts capturing the brittle behaviour of natural fractures (star-shaped points) and intact rock bridges (square-shaped points)

Two different constitutive models are applied in the analysis: one for the intact rock blocks and one for the block contacts. The intact blocks are assumed to be linear elastic, non-divisible and impermeable (see lower inset of Fig. 6). The contacts are discretized as either representing an existing fracture capable of tensile opening or shear slip, i.e., basal sliding zone, internal shear surface and natural fractures (schematized by star-shaped points in lower inset of Fig. 6 for natural fractures), or as an intact rock bridge vulnerable to tensile or shear failure (square-shaped points in lower inset of Fig. 6). A strain-softening Coulomb slip model is used in both cases with peak and residual strength values as listed in Table 3. The cohesion, friction and tensile strength are either assigned to be representative of open fractures or intact rock. This discretization strategy is referred as a “bonded-block approach”. Thus, damage and

**Table 3** Parametric inputs used in the groundwater flow and geomechanical models

Property	Unit	Value
Hydraulic conductivity, $K$ (m/s)	Aquitard	$2 \times 10^{-7}$
	Deep confined aquifer	$1 \times 10^{-6}$
Specific storage coefficient, $S_s$ (1/m)	Aquitard	$10^{-4}$
	Deep confined aquifer	$10^{-3}$
		Case (1)/Case (2)
Density, $\rho_r$ (kg/m <sup>3</sup> )	Rock mass	2600/2600
Elastic modulus, $E$ (GPa)	Fractured rock mass	10/10
	Intact rock	50/50
Poisson's ratio, $\nu$ (-)	Fractured rock mass	0.35/0.35
	Intact rock	0.25/0.25
Peak cohesion, $c_p$ (MPa)	Rock blocks	n/a (elastic)
	Basal/internal sliding zone/surface	0/0
	Sub-vertical and sub-horizontal natural fractures (Set 2 and 1)	2.5/1.0
	Intact rock bridges	5.0/5.0
Residual cohesion, $c_r$ (MPa)	Rock blocks	n/a (elastic)
	Basal/internal sliding zone/surface	0/0
	Sub-vertical and sub-horizontal natural fractures (Set 2 and 1)	1.0/0.1
	Intact rock bridges	2.5/0.5
Peak friction angle, $\phi_p$ (°)	Rock blocks	n/a (elastic)
	Basal/internal sliding zone/surface	30/30
	Sub-vertical natural fractures (Set 2)	40/40
	Sub-horizontal natural fractures (Set 1)	35/35
	Intact rock bridges	45/45
Residual friction angle, $\phi_r$ (°)	Rock blocks	n/a (elastic)
	Basal/internal sliding zone/surface	20/20
	Sub-vertical natural fractures (Set 2)	35/35
	Sub-horizontal natural fractures (Set 1)	30/30
	Intact rock bridges	25/25
Peak tensile strength, $T_p$ (MPa)	Rock blocks	n/a (elastic)
	Basal/internal sliding zone/surface	0/0
	Sub-vertical natural fractures (Set 2)	2.5/0.5
	Sub-horizontal natural fractures (Set 1)	5.0/0.5
	Intact rock bridges	10/0.5
Residual tensile strength, $T_r$ (MPa)	Rock blocks	n/a (elastic)
	Basal/internal sliding zone/surface	0/0
	Sub-vertical natural fractures (Set 2)	0/0
	Sub-horizontal natural fractures (Set 1)	0/0
	Intact rock bridges	0/0

progressive weakening of the slide mass in response to fluctuating pore pressures over time, is modeled as localized changes in effective stress that result in either the peak shear or tensile strengths of an intact rock bridge or an existing fracture being exceeded, resulting in the contact strength dropping to a residual value representative of a new plane of weakness (Fig. 7). The strain-softening

Coulomb slip model used for this is approximated by means of two linear segments as illustrated in Fig. 7, which assumes a brittle response in which the passing from peak to residual strength is sudden. Accordingly, failure of a rock bridge may facilitate slip or opening along an adjacent natural fracture, and vice versa, slip along an existing natural fracture may result in stressing and failure of an

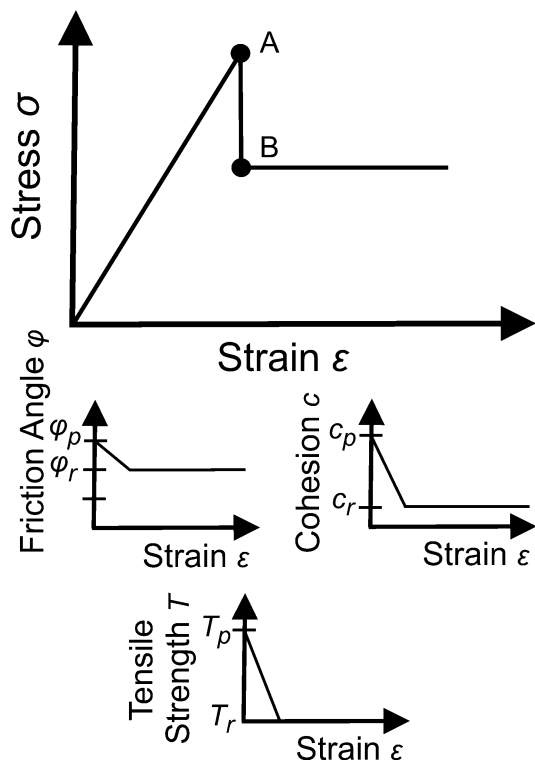


**Fig. 7** Strain-softening curve used in the numerical model, which assumes a sudden brittle response from peak (A) to residual strength (B), as applied to contact properties (friction angle, cohesion, tensile strength)

intact rock bridge. Failure of any discontinuity type is thus accompanied by: (i) a reduction in local resisting forces, and (ii) a change in the local kinematics of the landslide. Accordingly, increasing damage with time in response to fluctuating pore pressures may result in the incremental weakening of the modeled rock mass, i.e., fatigue, which in turn may lead to accelerating behaviour, both localized and global. This bonded-block approach implemented in UDEC (Itasca 2013) has been successfully used in several investigations of large complex rockslides (e.g., Eberhardt et al. 2004; Watson et al. 2006; Alzo'ubi et al. 2010; Gischig et al. 2015).

Boundary conditions of fixed zero normal velocity are specified along the side and bottom boundaries of the model domain (Fig. 5b). Before importing the series of pore pressure fields into the UDEC model, an in-situ stress field was initialized assuming gravity loading and a horizontal to vertical stress ratio of 0.5. Several observation points, identified in Fig. 5b, were introduced in the model in order to continuously monitor pore pressures, displacements, velocities and stresses.

The initial state of the landslide obtained after initialization of the in-situ stress, is subsequently perturbed by the superposition of the first pore pressure field in the series. 1000 calculation steps are performed to compute a

new state of the landslide. This value represents a sufficient number of calculation steps to compute the new state of the landslide in terms of stresses and displacements. This was repeated for each (14 day) pore pressure value for the 50 year modeling period. A customized subroutine was developed and implemented in UDEC using the internal programming language FISH to: (i) import pore pressure fields, (ii) link pore pressures generated at nodes in the 3-D groundwater model to fracture domains in the 2-D geomechanical model by means of a nearest-neighbor interpolation along section A–A' (see Figs. 3, 5), (iii) run the calculation of the new state of the landslide, and (iv) repeat the process over the 50 year period. At this point, it is important to note that in UDEC, the modeled movement velocity corresponds to slope movements over the number of calculation steps and not explicitly as true time. However, true time can be approximated given that 1000 calculation steps are performed for each new pore pressure field, which is imported at a time interval of 14 days. Calculated velocities are still treated here with caution as they can be affected by damping and mass scaling schemes used in UDEC to reduce computing times.

The model has been calibrated against measured displacements and velocities of Bonzanigo (1999), by fitting parametric inputs. Two different sets of rock properties, referred to here as Case (1) and Case (2), have been selected from the calibration phase; results from both cases are presented in the following section. Case (1) corresponds to higher strength rock mass properties reflecting unaltered crystalline rocks, while Case (2) assumes lower strength rock mass properties reflecting altered crystalline rocks. Table 3 specifies used rock properties, and used peak and residual values for the basal sliding zone, the internal shear surface, natural fractures and intact rock bridges for Case (1) and Case (2), respectively.

## 3.2 Results

### 3.2.1 Seasonal Fluctuation of Pore Pressures

Figure 8 shows the simulated (blue lines) and measured (black lines) pore pressures at different levels in borehole CVM6 for the period 1991–1997, based on the recharge time series imported into the model (see Fig. 3 for location of CVM6). The drop in measured pore pressures from 1995 onward is related to the construction of the drainage adit; the drainage adit is not included in the model simulation and therefore is not reflected in the modeled pore pressures. Modeled pore pressures match reasonably well with the measured values, especially close to the basal sliding zone where modeled pore pressures approach 2–2.5 MPa (Figs. 8, 9a).

**Fig. 8** Imposed recharge and simulated (*blue lines*) and measured (*black lines*) pore pressures as a function of time for borehole CVM6.

Superimposed gray intervals indicate periods of pressure fluctuation. The location of borehole CVM6 is shown in Fig. 3

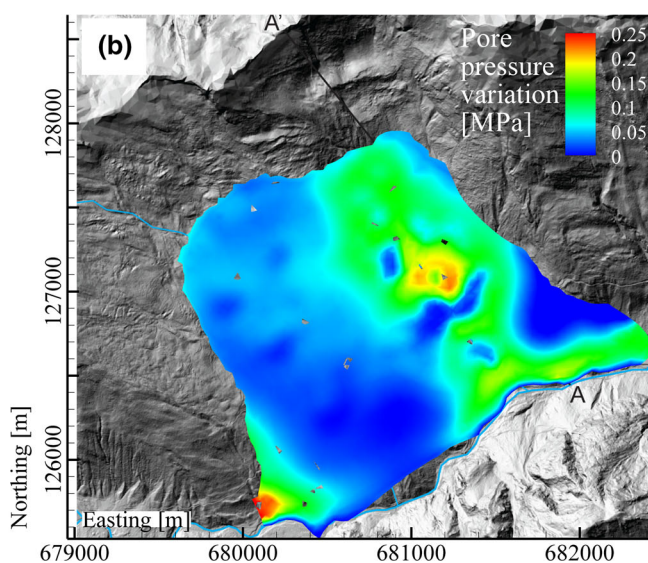
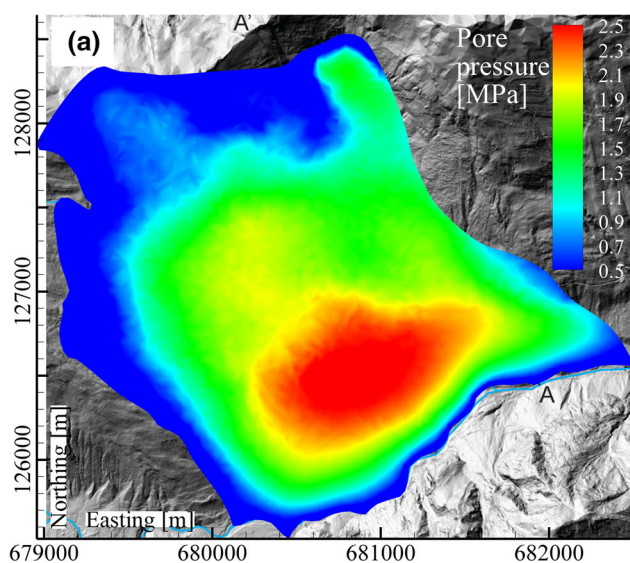
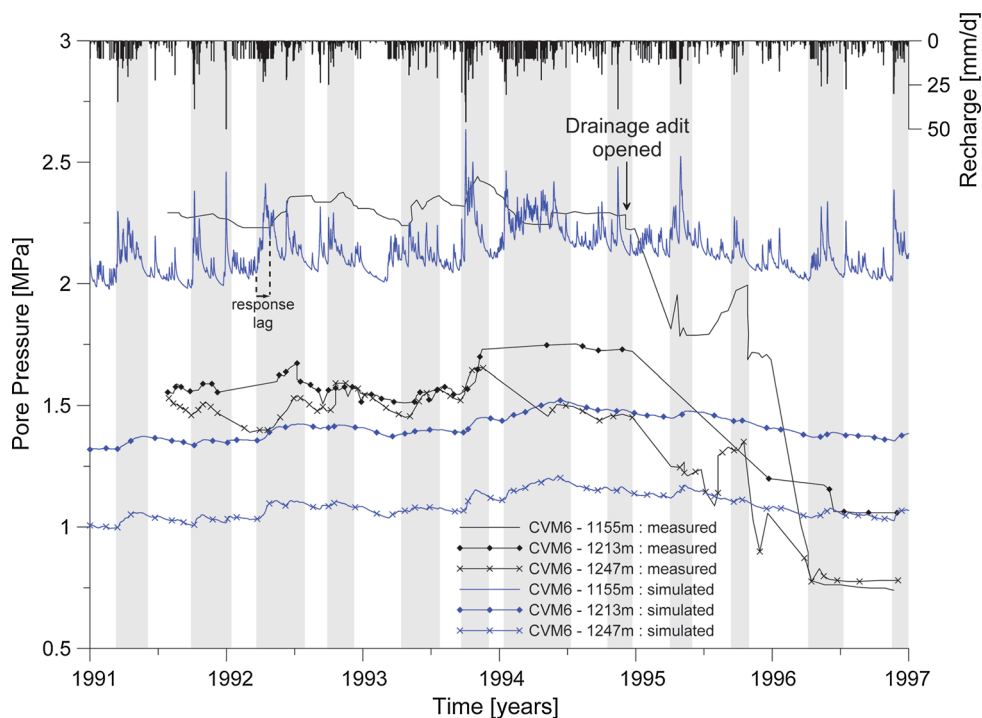


**Fig. 9** **a** Simulated pore pressures field across the base of the landslide during the hydraulic loading period of Fall 1993 (see Fig. 8). **b** Simulated pore-pressure variation between the high and low

pore pressures (peak-to-peak amplitude), close to the base of the landslide between the hydraulic loading periods of Fall 1993 and Winter 1993–1994

The gray bands superimposed on Fig. 8 highlight periods of high simulated pore pressures. These can be compared to periods of low pore pressure, which appear as white bands. Figures 8 and 9b show that the pore-pressure variation between these (peak-to-peak amplitude or fluctuation) is highest near the basal sliding zone with values varying by 0.25–0.5 MPa. This is in reasonable agreement with observed peak-to-peak amplitudes (Fig. 8). Two fluctuations

per year can be observed, corresponding to periods of spring snowmelt and autumn rains. As previously noted, the model is only recharged from its surface, which explains the rapid response of simulated pressures to recharge and the model's limited capacity to reproduce the response lag between recharge and increasing pressure. The time lag between measured and modeled pore pressures is indicated by an arrow in Fig. 8.

The simulated results were obtained with the hydrodynamic parameters presented in Table 3. These values are in line with measured data in Table 2 by Bonzanigo (1999). The hydraulic conductivity obtained for the deep aquifer matches the highest value measured in borehole CVM7, but remains low compared to values measured in borehole CVM4. The modeled pore pressures cover a period of 50 years (1961–2011) and constitute the basis of the hydromechanical analysis.

### 3.2.2 Slide Kinematics

The modeled slide kinematics are characterized by the lower part of the Campo slide body being more active than the upper part (Fig. 10). For both rock mass property cases, (1) and (2), the lower slide part experiences displacements of several centimeters associated with dextral shearing along the basal sliding zone (Fig. 10). In response, the modeled rock mass is subjected to significant internal shearing, dilation, rotation and wedging of intact blocks. With increasing time and hydromechanical (HM) cycling, a zone of high tensile strains develops between the upper and lower slide part resulting in the growth of sub-vertical tension cracks, and eventually, partial detachment of the lower section. Figure 10 shows both (a–c) the modeled shear displacement along the basal sliding zone and (b–d) modeled displacement vectors (color coded) after 10 and 25 years of hydromechanical cycling. The shear

displacement indicates the absolute shear movement along contact points (i.e., discontinuities and newly generated fractures); while the displacement vectors indicate the absolute movement that a gridpoint in the rock blocks accrued from the beginning of the HM fatigue analysis. These latter metrics integrate both shear displacements at the base and displacements within the sliding mass: slip of fractures and elastic deformation of rock blocks.

The kinematics of the lower slide part, despite having a somewhat flatter basal sliding zone angle, is more affected by the fluctuation of modeled pore pressures than the upper half of the slide. Still, movement of the upper slide accompanies the downslope slip of the lower slide in response to the decrease of resisting forces and opening of free space. This differential sliding along the basal shear zone between the upper and lower parts of the landslide in the one-way coupled HM UDEC model matches well with the geodetic monitoring data recorded at Campo Vallemaggia (see Bonzanigo et al. 2007), as well as with the numerical model presented in Eberhardt et al. (2007), which is based on a different modeling approach.

### 3.2.3 Episodic Slope Movement, Fatigue and Progressive Failure

As previously mentioned, pore pressure fields modeled in the deep confined aquifer are imported into the geomechanical model at a time interval of 14 days to simulate the

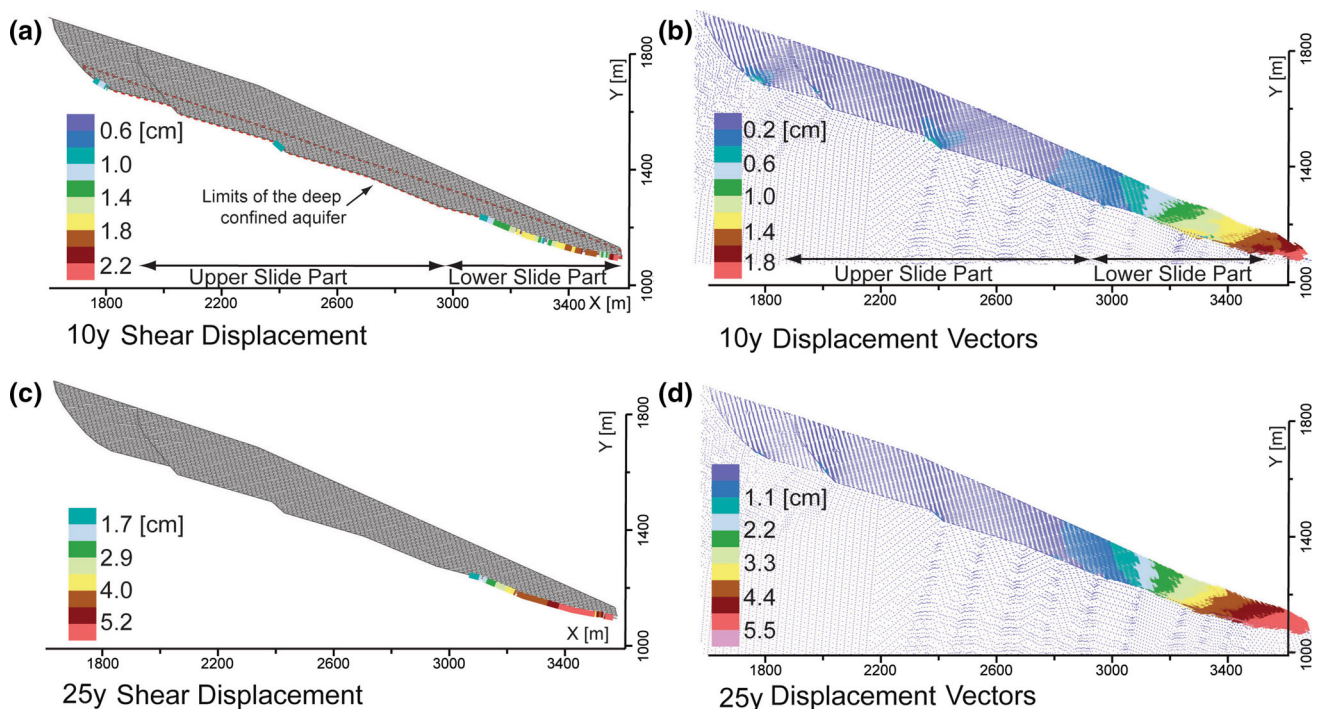


**Fig. 10** Case (1), simulated shear displacements along the basal sliding zone after **a** 10 years and **c** 25 years of hydromechanical cycling, and modeled state of the landslide (color coded displacement vectors) after **b** 10 years and **d** 25 years

hydromechanical response of the slope. Figure 11 shows simulated pore pressures (blue and green lines), velocities (red lines) and displacements (black lines) as a function of time for four different observation points, whose location is shown in Fig. 11. Observation points Lower Toe 1 (blue) and Lower Middle 1 (green) are located within the deep confined aquifer and thus experience pore pressure fluctuations. Observation points situated above the aquifer, Lower Toe 2 (red) and Lower Middle 2 (orange), show zero pore pressures. Note that pore pressure plots for the latter are not included. All observation points can be seen to be affected by the modeled pore pressure fluctuations regardless of their position (within or outside the deep confined aquifer). The slope responses assuming both cases of rock mass properties provided in Table 3 are presented in Fig. 11.

The general slide kinematics described in the previous section is also illustrated by the plots in Fig. 11, where for both cases, observation points located in the lower slide body (e.g., Lower Toe 1 and 2) are subject to peak velocities and displacements at least one order of magnitude higher than those for points located in the upper slide body (e.g., Lower Middle 1 and 2). For Case (1), the modeled slide velocities for the lower part of the slide seem more or less uniform regardless of the fluctuating pore pressures. Here, the displacements they cause are focused primarily along the basal sliding zone. In contrast, the modeled slide velocities for Case (2) are less uniform, particularly at the toe where the top of the sliding mass moves faster than the bottom. This non-uniform movement agrees with the inclinometer data reported by Bonzanigo et al. (2007) in borehole CVM6 for the Campo Vallemaggia body.

For both cases, peak velocities correlate with simulated pore pressure increases, which through localized fatigue are responsible for episodically increasing velocities from mm/year to cm/year. For Case (2) with lower strength properties, movement velocities at the observation point 'Lower Toe 2' are in the range of m/year, with a major acceleration phase of 2 cm/day characterized by a partial rupture at the landslide toe occurring after 17.5 years of cyclic loading. This rupture, resulting from the development of a major tensile failure zone, subsequently leads to detachment of the toe. This crisis of enhanced slope acceleration does not occur during the first substantial pore pressure loading, e.g., after 8 and/or 14 years, but happens during the third major pore pressure peak. This modeled behaviour and the range of simulated movement velocities are similar to the landslide acceleration crisis of 1993 (see Fig. 1a). This crisis was also accompanied by an observed major slide (detachment) in the landslide toe. Such crises, occurring during periods of substantial but not exceptional pore pressure loading, might indicate that the deep-seated

landslide is experiencing fatigue in response to cyclic effective stress perturbations and increasing damage. This behaviour is exhibited in Fig. 12 where the modeled fluctuation of pore pressures at 'Lower Toe 1' and the modeled displacement and velocity at 'Lower Toe 2' (see Fig. 11a for localization) are plotted as a function of time together with the occurrence of modeled damage (i.e., failed discontinuities within the slope). The first significant pore pressure fluctuations, e.g., at 2.5, 7.6 and 14 years, do not cause substantial accelerations of the modeled movement but promote the localized failure of numerous rock bridges and discontinuities, leading to increased damage. This then leads to a heightened acceleration phase (occurring at 17.5 years) in response to a substantial but not exceptional pore pressure increase. Note also that for Case (2) in Fig. 11, significant movements occur at the beginning of the simulation due to the introduction of varying pore pressures.

Case (1), assuming higher rock mass strength properties, is only affected by acceleration-deceleration phases concentrated along the basal sliding zone involving progressive failure of intact rock bridges (compare failed discontinuities between Fig. 13a, c). The importance of these accelerations is not always directly related to the amplitude of the modeled pore pressure variations (e.g., peak at 11 years in Fig. 11 for all the observation points of Case (1)); they mostly depend on the state of damage and fatigue affecting the intact rock bridges along the basal sliding zone. As illustrated by the UDEC model, the modeled seasonal fluctuation of groundwater pressure might weaken the landslide base via hydromechanical (HM) fatigue, leading to the progressive failure of intact rock bridges as they locally reach a critical stress level. At any given time, a small change in applied stress might be enough to cause failure of a highly damaged rock bridge, resulting in a landslide acceleration episode. Model results also indicate that shear strength degradation along the basal sliding zone happens retrogressively from the toe upslope into the slide body (Fig. 13a–d). Again, this also confirms that the kinematics of the upper slide strongly depends on the behaviour of the lower slide part.

Interestingly, despite the progressive weakening of the basal sliding zone, no major yielding, damage, or internal shearing occurs within the sliding body for Case (1). Figure 13 shows failed discontinuities at the initial state and after 30 years of HM cycling. Only a few failed discontinuities initiate for Case (1) within the slide body. These fractures nucleate and propagate from the basal sliding zone along the pre-defined sub-vertical discontinuities, in particular where intact rock bridges are situated along the basal sliding zone and attract localized stress concentrations. In contrast, substantial damage and internal shearing occurs within the lower slide body for the weaker rock

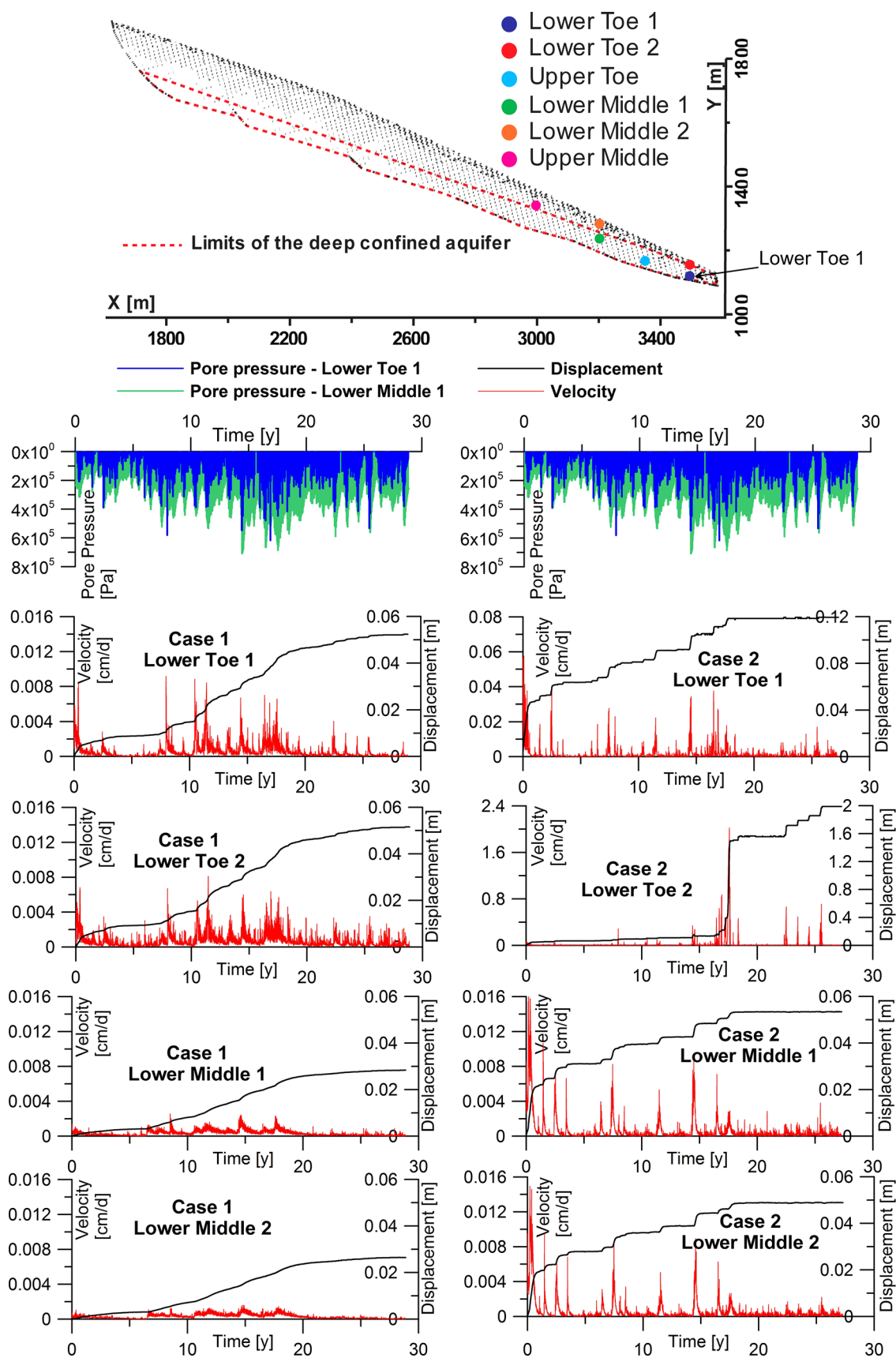


**Fig. 11** Modeled displacements (*black lines*), velocities (*red lines*) and pore pressure for (*left*) Case (1) and (*right*) Case (2). Input properties for Case 1 and 2 are provided in Table 3. Plots from *top to bottom* show results for the different observation points identified at the *top*. Note that initial time (year 0) commences with the regional precipitation records from 1961 (see *inset* in Fig. 5a)

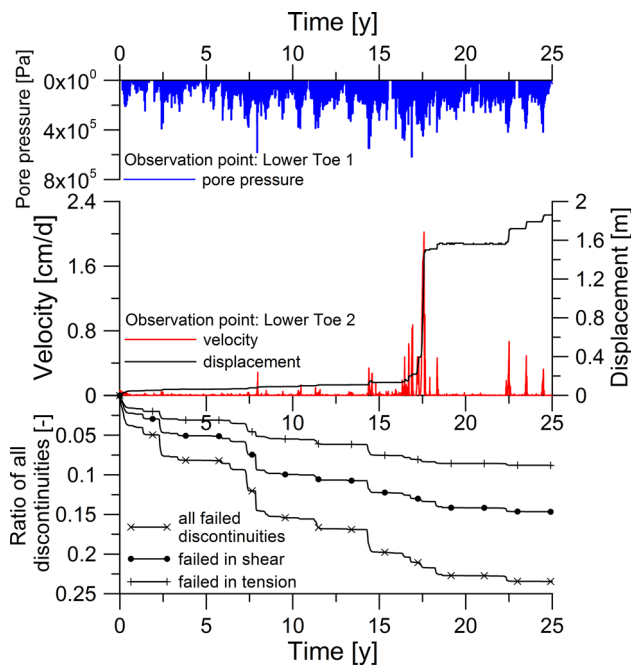


**Fig. 12** Modeled pore pressures at ‘Lower Toe 1’, simulated velocity and displacement at ‘Lower Toe 2’, as well as the ratio of failed discontinuities to total number of discontinuities, as a function of time. Refer to Fig. 11 for the location of observation points

mass assumption, Case (2) (Fig. 13b–d). Hydromechanical (HM) fatigue for this latter case is more effective, leading to progressive weakening not only along the basal sliding zone, but also within the lower sections of the slide (Fig. 13d). This results in sporadic acceleration events and crises of enhanced slope movement, as shown in Figs. 11 and 12, suggesting that the rock mass is suffering progressive failure and fatigue. Differences in the development of HM fatigue and damage between Cases (1) and (2) can be explained by the strength properties of natural fractures and intact rock bridges. The effectiveness of HM fatigue at the contact (fracture) scale is shown in Fig. 13e and f, where the stress paths for the specific contact of the six observation points are presented in the Mohr plot with peak and residual strength. For Case (1), HM cycling is responsible for normal (effective) stress fluctuations of about 0.25–0.5 MPa with no major shear stress modifications. The cycling affects fractures situated within the deeper confined aquifer zone (blue, cyan and green points in Fig. 13), and slow shear stress deviations are related to

stress redistribution due to local dislocation along the basal sliding zone. However, strength properties of pre-defined discontinuities in the sliding body are too high to be affected by the loading–unloading stresses. Under such conditions, rock mass degradation associated with HM fatigue remains limited to the basal sliding zone, as shown in Fig. 13c. For Case (2), the lower fracture and intact rock bridge strengths promote rupture events to occur, especially close to the basal sliding zone at the beginning of HM cycling (cyan point in Fig. 13f). These dislocated fractures weaken the deforming rock mass to its residual strength, leading to stress redistribution, as illustrated by the cyan, blue and pink curves in Fig. 13f. In such cases, rock degradation associated with HM fatigue extends also to the sliding rock mass and contributes to the formation of pockets with highly fractured rocks, as shown in Fig. 13d.

## 4 Discussion and Conclusions

Results presented in this paper demonstrate the key role that hydromechanical (HM) fatigue plays in the episodic movement and progressive failure of deep-seated landslides, using the Campo Vallemaggia landslide as an example. Each year, in response to the seasonal fluctuation of groundwater pressures, this landslide was subject to acceleration and deceleration phases with velocities ranging from a background of mm/year up to several cm/day (Fig. 1a). Occasionally these acceleration phases resulted in crisis responses by the local communities, such as in 1993. These episodes of extreme slope movement were not necessarily triggered by precipitation events of extraordinary amplitude, as would be expected from an effective stress limit equilibrium perspective. Instead, they suggest that HM fatigue contributes to localized slip and brittle fracture that in turn gradually weakens the rock mass contributing to progressive failure of the deep-seated landslide.

The principle of HM fatigue was demonstrated using distinct-element bonded-block modeling of the Campo Vallemaggia landslide. Cyclic fluctuations of modeled pore pressure were seen to cause critically stressed intact rock bridges along the basal sliding zone and within the slide body to fail. Once damage accumulated to a critical level locally, a subsequent stress perturbation of amplitude similar to previous pore pressure increases could trigger a significantly larger slope acceleration event (Fig. 12). This explains the capacity of a deep-seated landslide to remain at or near background levels of activity over extended periods of time, and then enter into a phase of critical acceleration. These reactivation periods are unpredictable and cannot be evaluated via static limit equilibrium analyses. Only advanced numerical models



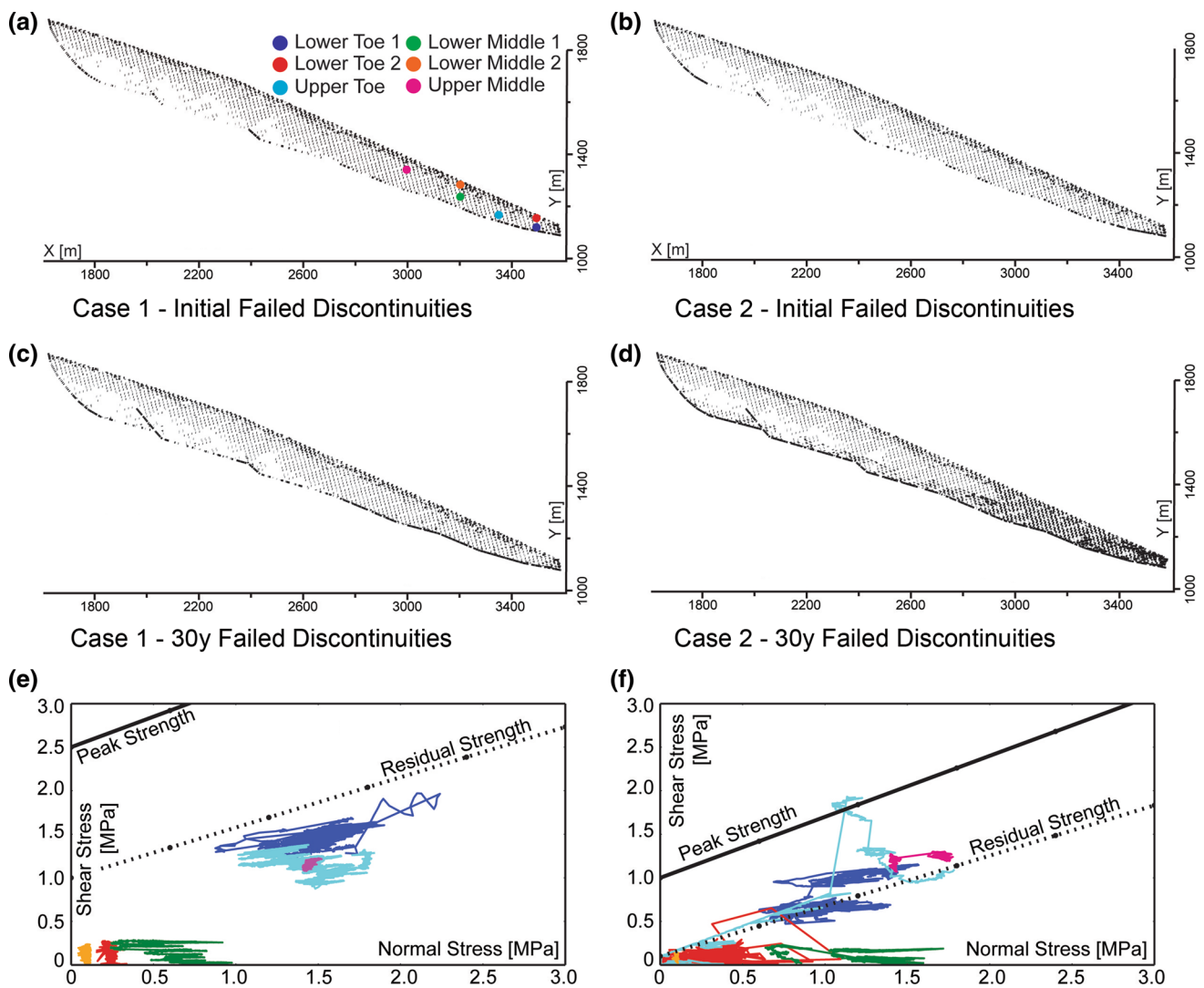


**Fig. 13** Model results for Cases 1 and 2 showing the failed discontinuities: **a, b** initially and **c, d** after 30 years of hydromechanical cycling. Also included are the stress paths in Mohr plot for the six observation points identified at the top of the figure for: **e** Case 1, and **f** Case 2

integrating damage and post-peak strength degradation behavior, calibrated against observed data, can provide assessments of intermittent slope movements and sensitivity to repeated acceleration events that may lead to forecasts of catastrophic failure potential. The numerical model presented in this paper represents an original approach to assessing the progressive failure of a deep-seated landslide under cyclic stress variations over long time intervals. At this point, it is interesting to note that Crosta et al. (2013) have recently published an inventory of 1033 deep-seated landslides in the Alps, of which 44 % are considered to be active. Many of these locate in populated areas and/or close to sensitive infrastructures (e.g., dams and reservoirs). Their long-term behaviour under the different type of rock mass fatigue (Table 1) could be

estimated by means of advanced numerical analyses, such as that presented in this work or in Gischig et al. (2015).

The modeling results have also illustrated that HM cycling contributing to fatigue and progressive failure is sensitive to the rock mass strength, as well as whether internal incremental damage with stress redistribution occurs somewhere in the deforming deep-seated slope. Thus, the effectiveness of HM fatigue to induce damage and further deteriorate an unstable rock slope highly depends on the local strength properties, as illustrated by Case (2) in the analysis presented. It should be noted that in some cases, the deformation characteristics of a rock slope may remain in an approximate elastic state, leading to only reversible deformations associated with the fluctuation of pore pressures (and opening and closing of water filled

fractures), such as the rock slope behaviour observed in Hansmann et al. (2012).

Also presented here is a one-way coupled HM formulation to model intermittent landslide behaviour as is typically observed in deep-seated landslides. In the example of Campo Vallemaggia, there exist more than 100 years of observations of intermittent landslide activity. Despite several of these re-activation periods reaching crisis levels, the landslide has never reached a state of rapid catastrophic failure. Thus, a fundamental open question is whether HM fatigue could lead to a rapid catastrophic rupture. With the progression of time and number of cycles, as well as whether the kinematics of the sliding surface contribute to self-stabilization or not, the interaction between driving and resisting forces could result in a catastrophic failure event as shown by Gischig et al. (2015). The post-failure model implemented in these analyses implies a reduction in local rock mass strength from peak to residual, resulting in an overall reduction of resisting forces. This in turn results in displacements that then locally modify the geometry of the landslide body relative to the basal sliding zone. Indeed, any geometry change due to a movement along a concave sliding path, as is the case for many deep-seated landslides involving more gradual slope angles, will result in a decrease of the driving forces associated with self-weight and gravity loading. For the cases reported in Gischig et al. (2015), steeper slopes enabled by strong crystalline rock favor a brittle collapse failure mode, as defined by Hungr et al. (2014), which produces a sudden catastrophic failure event. Contrary, deep-seated landslides having a concave sliding path, such as Campo Vallemaggia (Bonzanigo 1999), La Frasse in Vaud, Switzerland (Tacher et al. 2005), or La Clapière in Alpes-Maritimes, France (Hungr and Evans 2004), have all been affected by pore pressure fluctuations for hundreds if not thousands of years but have yet to fail catastrophically. For instance, the total deformation of La Clapière is on the order of 100 m, but velocities never exceeded values greater than several cm/day. Based on the aforementioned points, it seems unlikely that HM cycling alone can lead to the catastrophic failure of a large rock slope over shorter intervals of time. However, if hydromechanical (HM) cycling follows or acts in combination with another major large-scale process affecting the slope's load history, for example, an earthquake event, then HM fatigue can be exceptionally effective in accelerating progressive failure of the slope. Gischig et al. (2015), in a companion paper to this one, investigate rock mass fatigue due to a sequence of earthquakes (seismic fatigue), applying HM cycling after a given event. They observed that HM cycling applied after a series of damaging earthquakes results in the modeled rock slope suffering fatigue at a faster rate. This observation is in good agreement with our previously presented findings.

Large-scale stress perturbations such as glacial unloading processes (Eberhardt et al. 2004) and seismic activity (Gischig et al. 2015), are less frequent than hydromechanical (and thermomechanical) cycling, but they represent major perturbations to the entire slope's stress conditions. Once generated, the increase in fracture dilation and connectivity results in increased permeability and the beginning or the acceleration of the HM fatigue process. This general conceptual model of fatigue is not restricted to the Campo Vallemaggia landslide, but it can also be invoked for other large rock slope instabilities, such as that at Randa, Switzerland (Eberhardt et al. 2004; Gischig et al. 2011). Likewise, HM fatigue is not restricted to natural cyclic fluctuations of groundwater pressures but would also apply to anthropogenic sources such as those occurring with hydroelectric reservoirs (Zangerl et al. 2010).

The modeling approach presented is based on the assumption that hydrodynamic parameters do not change with the movement of the deep-seated landslide. However, it is well accepted that fracture aperture and permeability increase with shear dilation, as well as rock permeability and porosity increase with fragmentation. This increase in rock mass permeability and porosity with the intermittent movement of a deep-seated landslide may result in a slow decrease of peak pore pressure fluctuations over time. Thus conceptually, over long periods of time, it becomes more difficult to induce critical pore pressures, leading to less frequent reactivation phases. Future studies on episodic movement and hydromechanical fatigue need to examine such aspects in order to assess the long-term behaviour of deep-seated landslides, as well as the consideration of 3-D pressure distributions and displacements. Further research integrating field investigations and back-analysis by advanced numerical modeling is also necessary to assess the role of different types of fatigue in the progressive failure of a deep-seated landslide.

**Acknowledgments** The authors wish to thank the anonymous reviewers whose comments have helped to improve this paper, as well as Prof. K. Hutter for a careful review. Financial support of this research has been provided by the Swiss National Science Foundation (Project No. 146075) and a Natural Sciences and Engineering Research Council of Canada Discovery Grant.

## References

- Alzo'ubi AK, Martin CD, Cruden DM (2010) Influence of tensile strength on toppling failure in centrifuge tests. *Int J Rock Mech Min Sci* 47:974–982
- Bonzanigo L (1999) Lo slittamento di Campo Vallemaggia. PhD thesis, ETH Zurich, Switzerland
- Bonzanigo L, Oppizzi P, Tornaghi M, Uggeri A (2006) Hydrodynamics and rheology: key factors in mechanisms of large landslides. In: *Proceedings geohazards engineering conferences international*, Lillehammer, Norway, 18–21 June 2006

- Bonzanigo L, Eberhardt E, Loew S (2007) Long-term investigation of a deep-seated creeping landslide in crystalline rock. Part I: Geological and hydromechanical factors controlling the Campo Vallemaggia landslide. *Can Geotech J* 44(10):1157–1180
- Cornaton FJ (2014) Ground water: a 3-D ground water and surface water flow, mass transport and heat transfer finite element simulator. Reference manual. Centre for Hydrogeology and Geothermics, Neuchâtel
- Crosta GB, Frattini P, Agliardi F (2013) Deep seated gravitational slope deformations in the European Alps. *Tectonophysics* 605:13–33
- Cundall PA, Hart RD (1992) Numerical modelling of discontinua. *Eng Comput.* 9:101–113
- Eberhardt E (2008) Twenty-ninth Canadian geotechnical colloquium: the role of advanced numerical methods and geotechnical field measurements in understanding complex deep-seated rock slope failure mechanisms. *Can Geotech J* 45(4):484–510
- Eberhardt E, Stead D, Coggan JS (2004) Numerical analysis of initiation and progressive failure in natural rock slopes—the 1991 Randa rockslide. *Int J Rock Mech Min Sci* 41:69–87
- Eberhardt E, Bonzanigo L, Loew S (2007) Long-term investigation of a deep-seated creeping landslide in crystalline rock. Part II: Mitigation measures and numerical modelling of deep drainage at Campo Vallemaggia. *Can Geotech J* 44(10):1181–1199
- Furuya G, Sassa K, Hiura H, Fukuoka H (1999) Mechanism of creep movement caused by landslide activity and underground erosion in crystalline schist, Shikoku Island, southwestern Japan. *Eng Geol* 53(3–4):311–325
- Gischig VS, Moore JR, Evans KF, Amman F, Loew S (2011) Thermomechanical forcing of deep rock slope deformation: 2. The Randa rock slope instability. *J Geophys Res.* doi:10.1029/2011JF002007
- Gischig VS, Preisig G, Eberhardt E (2015) Numerical investigation of seismically-induced rock mass fatigue as a mechanism contributing to the progressive failure of deep-seated landslides. *Rock Mech Rock Eng* (this issue)
- Goodman RE (1980) Introduction to rock mechanics. Wiley, New York
- Hansmann J, Loew S, Evans K (2012) Reversible rock-slope deformations caused by cyclic water-table fluctuations in mountain slopes of the Central Alps, Switzerland. *Hydrogeol J* 20(1):73–91
- Harby A, Sauterleute J, Korpas M, Killingtveit A, Solvang E, Nielsen T (2013) Pumped storage hydropower. In: Stolten D, Scherer V (eds) Transition to renewable energy systems, pp 597–618
- Heim A (1932) Bergsturz und Menschenleben. Fretz and Wasmuth, Zurich
- Hendron AJ, Patton FD (1985) The Vaiont slide, a geotechnical analysis based on new geologic observations of the failure surface. In: Technical report GL-85-5, vol I, II. Department of the Army US Army Corps of Engineers, Washington DC
- Hsiung SM, Chowdhury AH, Nataraja MS (2005) Numerical simulation of thermal-mechanical processes observed at the drift-scale heater test at Yucca Mountain, Nevada, USA. *Int J Rock Mech Min Sci* 42:652–666
- Hungr O, Evans SG (2004) The occurrence and classification of massive rock slope failure. *Felsbau (Vienna, Austria)* 22:16–23
- Hungr O, Leroueil S, Picarelli L (2014) The Varnes classification of landslide types, an update. *Landslides* 11(2):167–194
- Itasca (2013) UDEC 5.0 universal distinct element code. Itasca Consulting Group, Minneapolis
- Kilburn CRJ, Petley DN (2003) Forecasting giant, catastrophic slope collapse: lessons from Vajont, Northern Italy. *Geomorphology* 54:21–32
- Leith K, Moore JR, Amman F, Loew S (2014) Subglacial extensional fracture development and implications for Alpine valley evolution. *J Geophys Res Earth Surf* 119:62–81
- Leroueil S, Vaunat J, Picarelli L (1996) A geotechnical characterization of slope movements. In: Proceedings of the 7th international symposium on landslides, Trondheim, vol 1, pp 53–74
- Löw S (1997) Wie sicher sind geologische Prognosen? *Bull Angew Geol* 2(2):83–97
- Macfarlane DF (2009) Observations and predictions of the behaviour of large, slow-moving landslides in schist, Clyde Dam reservoir, New Zealand. *Eng Geol* 109(1–2):5–15
- Min K-B, Rutqvist J, Tsang C-F, Jing L (2004) Stress-dependent permeability of fractured rock masses: a numerical study. *Int J Rock Mech Min Sci* 41:1191–1210
- Müller L (1964) The rock slide in the Vaiont valley. *Rock Mech Eng Geol* 2:148–212
- Müller L (1987) The Vajont catastrophe—a personal review. In: Leonards GA (ed) Dam failures. Engineering geology, vol 24(1–4), pp 423–444
- Parriaux A, Bonnard C, Tacher L (2010) Glissements de terrain: hydrogéologie et techniques d'assainissement par drainage. In: Guide Pratique. Office Fédéral de l'Environnement (OFEV), Bern
- Pedrazzini A, Jaboyedoff M, Loye A, Derron MH (2013) From deep seated slope deformation to rock avalanche: destabilization and transportation models of the Sierre landslide (Switzerland). *Tectonophysics* 605:149–168
- Preisig G, Cornaton FJ, Perrochet P (2012) Regional flow simulation in fractured aquifers using stress-dependent parameters. *Groundwater* 50(3):376–385
- Preisig G, Dematteis A, Torri R, Monin N, Milnes E, Perrochet P (2014) Modelling discharge rates and ground settlement induced by tunnel excavation. *Rock Mech Rock Eng* 47:869–884
- Preisig G, Eberhardt E, Gischig V, Roche V, Van der Baan M, Valley B, Kaiser P, Duff D, Lowther R (2015) Development of connected permeability in massive crystalline rocks through hydraulic fracture propagation and shearing accompanying fluid injection. *Geofluids.* doi:10.1111/gfl.12097
- Selli R, Trevisan L, Carloni CG, Mazzanti R, Ciabatti M (1964) La frana del Vajont. In: *Giornale di Geologia, serie 20, XXXII(I)*, pp 1–154
- Tacher L, Bonnard Ch, Laloui L, Parriaux A (2005) Modelling the behaviour of a large landslide with respect to hydrogeological and geomechanical parameter heterogeneity. *Landslides* 2(1):3–14
- Vuillet L, Hutter K (1988) Viscous-type sliding laws for landslides. *Can Geotech J* 25:467–477
- Watson AD, Moore DP, Stewart TW (2004) Temperature influence on rock slope movements at checkerboard creek. In: Proceedings of the 9th international symposium on landslides, Rio de Janeiro, vol 2, pp 1293–1298
- Watson AD, Martin CD, Moore DP, Stewart TWG, Lorig LJ (2006) Integration of geology, monitoring and modelling to assess rockslide risk. *Felsbau* 24:50–58
- Zangerl C, Eberhardt E, Perzlsmaier S (2010) Kinematic behaviour and velocity characteristics of a complex deep-seated crystalline rockslide system in relation to its interaction with a dam reservoir. *Eng Geol* 112:53–67